# Directivity in NGA Earthquake Ground Motions: Analysis Using Isochrone Theory

**Paul Spudich,**[a] M.EERI, **and Brian S. J. Chiou**[b]

We present correction factors that may be applied to the ground motion prediction relations of Abrahamson and Silva, Boore and Atkinson, Campbell and Bozorgnia, and Chiou and Youngs (all in this volume) to model the azimuthally varying distribution of the GMRotI50 component of ground motion (commonly called "directivity") around earthquakes. Our correction factors may be used for planar or nonplanar faults having any dip or slip rake (faulting mechanism). Our correction factors predict directivity-induced variations of spectral acceleration that are roughly half of the strike-slip variations predicted by Somerville et al. (1997), and use of our factors reduces record-to-record sigma by about 2–20% at 5 sec or greater period.
[DOI: 10.1193/1.2928225]

## INTRODUCTION

In a landmark paper Somerville et al. (1997) (henceforth SSGA) demonstrated the correlated effects of rupture propagation, earthquake source radiation pattern, and particle motion polarization on near-source ground motions. Their combined effect has subsequently been referred to in the engineering literature as "directivity," although in the seismological literature this term is reserved exclusively for rupture propagation effects. For use in predicting ground motion amplification, duration, and polarizations SSGA introduced two predictor variables, $X\cos(\theta)$ for vertical strike-slip faults and $Y\cos(\phi)$ for dip slip faults (see SSGA for definitions).

Despite the importance of SSGA's advance, use of their formulation has led to some practical and conceptual difficulties. On the practical side, their formulation is a discontinuous (step) function of magnitude, fault dip, fault rake, and rupture distance. Their formulation does not predict ground motions in an excluded zone (called the neutral zone below) around dipping faults, nor is its application to nonplanar faults clear. On the conceptual side, there is only weak theoretical justification for their functional forms. For long strike-slip faults, their $X$ factor implies that ground motion increases progressively along a rupture all the way to its end, a prediction clearly in conflict with the intensity map from the 1906 San Francisco earthquake (Boatwright and Bundock 2008). Abrahamson (2000) has modified the SSGA model to avoid some of these problems by capping $X\cos(\theta)$ at 0.4 and by introducing magnitude- and distance-tapers to smooth discontinuities. Rowshandel (2006) has cleverly generalized both the $X$ and $\theta$ terms to

[a] U.S. Geological Survey, 345 Middlefield Road, Menlo Park, CA 94025
[b] California Department of Transportation, 5900 Folsom Blvd., Sacramento, CA 95819


*Earthquake Spectra,* Volume 24, No. 1, pages 279–298, February 2008; © 2008, Earthquake Engineering Research Institute

smooth and extend the range of applicability of the basic SSGA model, at the price, however, of requiring a surface integral to be done over the fault for every receiver location.

This paper has the following goals. 1) We wish to develop physically-based predictor variables by using isochrone theory (Bernard and Madariaga 1984; Spudich and Frazer 1984, 1987). We attempt to keep these predictors as simple and computationally rapid as possible while retaining essential physics and limiting the domain of applicability as little as possible. 2) Using this theory, we clarify the various factors that contribute to azimuthal distribution of shaking around a source. 3) We develop directivity models with empirically determined coefficients that can be used to calculate a "directivity" correction to each NGA developer's ground motion prediction model.

## DEFINITION OF ISOCHRONE DIRECTIVITY PREDICTOR, *IDP*

Isochrone theory allows a simplification of an otherwise complicated formulation in computational seismology. The theory simplifies the computation of synthetic seismograms to an analytical expression, from which one can identify the main contributors to directivity effects (or the azimuthal variation of near-fault ground motion). In the isochrone formulation three main contributors to the azimuthal variation of ground motions are recognized. These factors, which various formulations lump together under the term "directivity," include the slip distribution, the radiation patterns, and true seismic directivity (in its guise here as isochrone velocity). In the last few years we experimented with numerous candidate variables and functional forms to search for a preferred representation of these three contributors for the purpose of modeling directivity effects in a (even simpler) ground-motion prediction model. Some of our earlier efforts are documented in Spudich et al. (2004) and Spudich and Chiou (2006). In the following we present and justify this preferred predictor variable and compare it to the predictor variables used by SSGA.

Our preferred predictor of directivity effects, *IDP* (the isochrone directivity predictor), is a product of three terms

$$IDP = CSR_{ri}, \tag{1}$$

$$C = \frac{\min(\tilde{c}', 2.45) - 0.8}{(2.45 - 0.8)} \tag{2}$$

$$S = \ln[\min(75, \max(s, h))] \tag{3}$$

All the above terms are evaluated at a site $\mathbf{x}_s$ in the geometry shown in Figure 1, in which $s$ is the along-strike distance in km from the hypocenter $\mathbf{x}_h$ to the point $\mathbf{x}_c$ on the fault closest to the site, and $h$ is the downdip distance in km from the top of the rupture to the hypocenter. Approximate isochrone velocity ratio $\tilde{c}'$ is defined below. $C$ is a normalized form of $\tilde{c}'$, lying in the range $[0, 1]$. $R_{ri}$ is a scalar radiation pattern amplitude defined below, ranging from 0 to about 1, which we use for the GMRotI50 component of motion. More discussions of the definitions of $S$ and $C$ are given in the next section. In

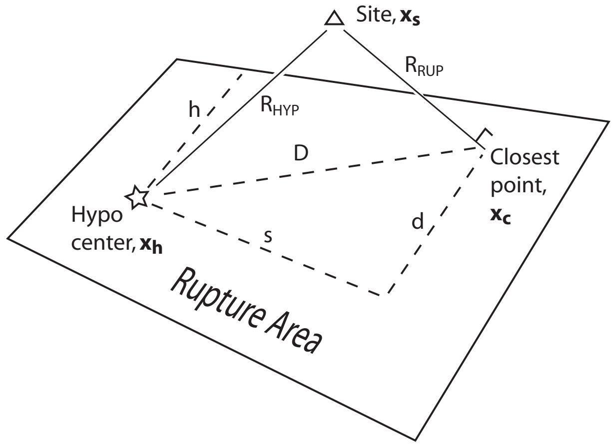


**Figure 1.** Rupture and site geometry.

Equation 1, $S$ takes the role of $X$, and $C$ takes the role of $\cos(\theta)$ in $X\cos(\theta)$. The radiation pattern amplitude $R_{ri}$ provides the neutral region defined by SSGA for reverse events. Equation 1 differs from the functional form recommended by Spudich et al. (2004). We will comment on this later.

Isochrone velocity ratio $\tilde{c}'$ is an approximation of the isochrone velocity defined in Spudich and Frazer (1984), which captures the seismic directivity amplification around a fault. It has the advantages of being defined everywhere on the Earth's surface around vertical and dipping faults using distance measures obtainable in typical practice. Spudich et al. (2004) defined $\tilde{c}'$ to be proportional to the distance $D$ (Figure 1) between the hypocenter and the closest point, divided by the difference in arrival times of S waves from these two points. The physical meaning is simple; all the energy radiated between the hypocenter and the closest point arrives in a time interval, and if that time interval is very short energies are time-compressed, a directivity pulse is formed, and the spectral amplitude is amplified.

$\tilde{c}'$ is derived in Electronic Appendix A (Spudich and Chiou 2008), and is given by

$$\tilde{c}' := \left(\frac{\beta}{v_r} - \frac{(R_{HYP} - R_{RUP})}{D}\right)^{-1}, \quad D > 0, \quad \tilde{c}' = \frac{v_r}{\beta}, \quad D = 0 \tag{4}$$

where rupture velocity is $v_r$ and $\beta$ is the shear wave speed in the source region. In this work we assume

$$v_r/\beta = 0.8,$$

which, on average, is a good approximation for most earthquakes. Note that $\tilde{c}'$ depends only on the locations of the hypocenter, the site, and the point on the fault closest to the site. $\tilde{c}'$ lies in the range

$$\frac{v_r}{\beta} \le \tilde{c}' \le \left(\frac{\beta}{v_r} - 1\right)^{-1}$$

which, for $v_r/\beta = 0.8$ is the range from 0.8 to 4. For a fault having bilateral rupture $\tilde{c}'$ achieves its maximum value when the rupture is traveling directly toward the site, and it achieves the above minimum value when the rupture direction is exactly *perpendicular* to the direction to the site. Spudich et al. (2004)'s main results (their Equations 9a and 9b, which we use here) assumed that the earthquake's hypocenter is not on the edge of the fault. Their special case of a hypocenter exactly on the edge of a fault (their Equation 10) is not used here. The $D=0$ limit of $\tilde{c}'$ (Equation 4) is multivalued when the hypocenter is on the edge of the rupture area, and consequently we recommend that hypocenters not be placed on the edge of rupture areas. Guidelines for sensible placement of hypocenters can be found in Mai et al. (2005). For multisegment faults, we generalize $s$ and $D$ as shown in Electronic Appendix A (Spudich and Chiou 2008).

Finally, scalar radiation pattern $R_{ri}$ is

$$R_{ri} = \max\left(\sqrt{R_u^2 + R_t^2}, \varepsilon\right),$$

where $R_t$ and $R_u$ are the strike-normal (transverse) and strike-parallel hypocentral radiation patterns (Electronic Appendix A (Spudich and Chiou 2008)), with a water level $\varepsilon = 0.2$ filling the nodes. We approximate the finite fault radiation pattern by a single point source radiation pattern. Electronic Appendix A (Spudich and Chiou 2008) describes a generalization for use with multisegment ruptures and it gives a computed example.

## DIRECTIVITY IN SYNTHETIC DATA

Despite having 3551 records from 173 earthquakes, there are very few earthquakes in the NGA dataset that are recorded at 10 or more azimuthally well-distributed stations having good data at long periods where the directivity signal is strongest. In addition, the azimuthal distribution of ground motion around these events, particularly at rupture distances less than 40 km, is strongly correlated with the local slip distribution. In such cases it is difficult to separate the effects of true directivity from the effects of proximity to a local slip maximum, making the inference of directivity effects very problematic.

Consequently, we turned to the rich data set of synthetic data calculated by the URS Corporation to provide guidance on the search for preferred predictor variable and an effective functional form for a directivity model. URS calculated synthetic strike-normal and strike-parallel seismograms at about 200 station locations surrounding 10 strike-slip events and 12 reverse-slip events, described in Abrahamson (2003) and Somerville et al. (2006). We used a subset of the events (Table 1) with deeper hypocenters located 10%, 30%, and 50% of the fault length from a fault edge.

Because synthetic data contain effects like magnitude scaling and geometric spreading in addition to directivity, we had to remove from the data the nondirective part of the motions. This is done by fitting simulated data from each event and each hypocenter location to a simple nondirective model

**Table 1.** Synthetic URS events used

| Event Name | Mag | W (km) | L (km) | Dip (dg) | Top of Rupture (km) |
|---|---|---|---|---|---|
| RB | 6.5 | 18 | 18 | 45 | 0 |
| RG | 7.0 | 28 | 36 | 45 | 0 |
| RK | 7.5 | 28 | 113 | 45 | 0 |
| SA | 6.5 | 13 | 25 | 90 | 0 |
| SD | 7.0 | 15 | 67 | 90 | 0 |
| SE | 7.5 | 15 | 210 | 90 | 0 |
| SH | 7.8 | 15 | 420 | 90 | 0 |

$$\ln(y_i) = k_1 + k_2 \ln(R_{RUP_i} + k_3) + \rho_i$$

where $y_i$ was the GMRotI50 spectral acceleration at station $i$, $R_{RUP_i}$ was the closest distance to the fault from station $i$, $\rho_i$ is the residual, and $k_i$ are unknown coefficients determined by regression analysis. We then used the residuals $\rho_i$, referred to as the "directive residual" below and shown in Figure 2, to guide the development of our directivity model.

We examined the correlation of directive residuals with a variety of candidate predictors motivated by the isochrone theory. Spudich et al. (2004) noted that the logarithm of the ground motion should be proportional to the logarithm of isochrone velocity ratio $\tilde{c}'$, and Spudich and Chiou (2006) proposed that the predictor should contain the product $\ln(\tilde{c}'\bar{D})$, where $\bar{D}$ is $D$ normalized by the diagonal of the fault. In the current work we further tested various products of log or linear $\tilde{c}'$ and $\bar{D}$ against the directive residuals. Following Abrahamson and Silva (2007) we also tested forms involving $s$ and $\ln(s)$. Below is a summary of our findings and decisions that ultimately lead to the definitions of $C$ and $S$ given in Equations 2 and 3.

We noted that the directive residuals correlated well with $\tilde{c}'$ up to a value of 2.45, which prompted us to cap $\tilde{c}'$ at 2.45. We decided to normalize the capped $\tilde{c}'$ so the resulting variable, $C$ of Equation 2, is in the range $[0,1]$, same as the $\cos(\theta)$ and $\cos(\phi)$ used by SSGA. We also noted the correlation of directive residuals with $\ln(s)$ was more linear than with either $\bar{D}$ or $s$. Based on the above two observations, we speculated that a predictor involving the term $C\ln(s)$ would work well for modeling the directivity effect in URS's simulated motions. This is confirmed by the plots in Figure 2, which show the correlation of directive residuals with $C\ln(s)$ for both the strike-slip and reverse events listed in Table 1. The residuals are a linear function of $C\ln(s)$ between about 0 and 4. Note that within the interval $[0,4]$ the slope of the residuals is about the same over the magnitude range 6.5–7.8 and for strike-slip and reverse events. Note also that residuals from hanging wall, foot wall, and neutral zone stations (zones defined in the NGA database documentation) show the same approximate slope with respect to $C\ln(s)$.

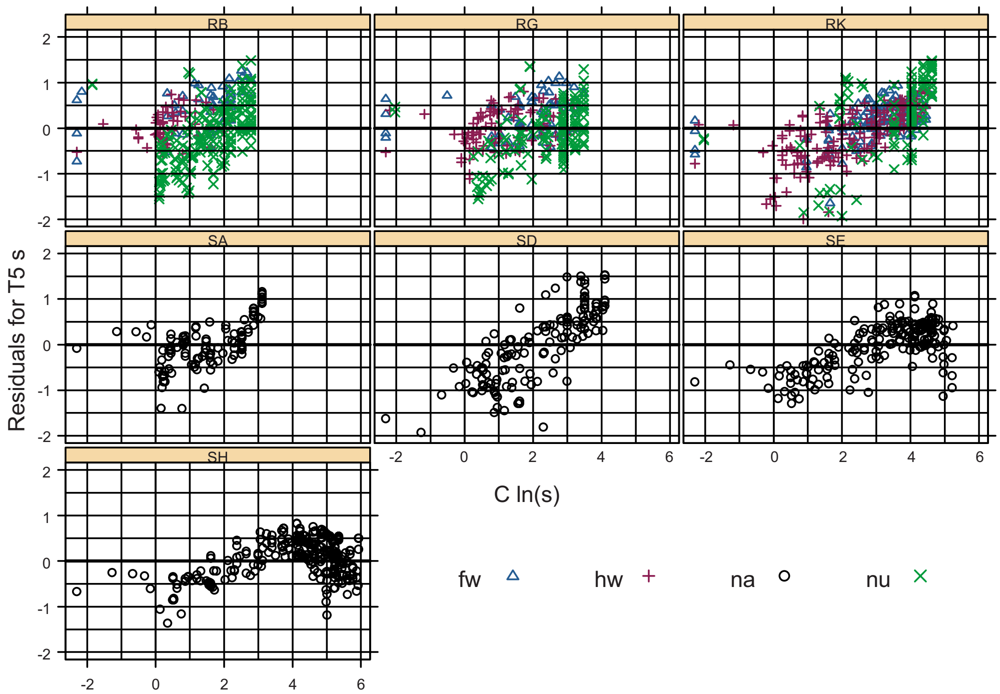


**Figure 2.** URS directive residuals for 5 sec period, as a function of $C\ln(s)$ for reverse events RB, RG, RK, and strike-slip events SA, SD, SE, and SH (Table 1). Symbols: ($\triangle$) footwall stations, (+) hanging wall stations, ($\times$) neutral zone stations, and ($\bigcirc$) other stations (strike-slip faulting stations).

Other tested predictors did not share these characteristics. Some magnitude dependence is seen in the average level of the residuals, but no magnitude dependence was seen in the real earthquake data.

From Figure 2 it was obvious that some modifications to $C\ln(s)$ were needed in order to model the directive residuals outside the interval $[0,4]$. For negative predictor values a horizontal tail of residuals indicates that a floor of 1 km should be placed under $s$. However, with this floor value the form $C\ln(s)$ produces no directivity directly up-dip from the hypocenter of a reverse event (because $\ln(s)$ is 0), a behavior that is contradictory to SSGA and not supported by the (limited) data in both simulations and the NGA dataset. A proper floor (larger than 1 km) is needed to allow up-dip directivity to come through. We picked $h$ (the downdip distance in km from the top of the rupture to the hypocenter; Figure 1) to be the floor of $s$. With this floor our updip prediction is improved, but still underestimates the empirical data by about 0.2 ln units. See Appendix D (Spudich and Chiou 2008) for plots of updip residuals.

The strike-slip residuals decline for $C\ln(s)$ value greater than 4, but we chose not to include this decline in our model. These residuals correspond primarily to higher values of *s*, meaning that they are farther down the rupture. A decline in spectral acceleration with distance along long strike-slip ruptures was seen, not only in the URS synthetics, but also in synthetic ground motions produced by Pacific Engineering and Analysis (Somerville et al. 2006) and by ourselves (not shown). The decline does not seem to be caused by the diminution of slip toward the end of the rupture. We chose not to include this decline in our model because we do not yet understand the cause of the decline, and not understanding the cause, we cannot be confident that such a variation in spectral acceleration seen in synthetic seismograms would be found in real motions from long strike-slip earthquakes. Consequently, in our model we cap *s* at a value of 75 km, derived from our synthetic ground motions, meaning that like Abrahamson (2000), our predictor does not continue to rise inexorably with distance along the rupture. However, by capping rather than tapering to zero for very large *s*, our predictor might overpredict directivity effect at the ends of very long strike-slip ruptures.

## EMPIRICAL DATA

We used the same record selection criteria as did each developer. Developer teams in this volume, Abrahamson and Silva (2008), Boore and Atkinson (2008), Campbell and Bozorgnia (2008), and Chiou and Youngs (2008) (AS, BA, CB, and CY in the following) provided us with their predicted ground motions for their selected records, from which we derived total residuals (observed ground motion minus developer's median prediction). If the developer provided a predicted motion for an NGA record, we used the record. Developer's total residuals were the "response data" used in our regression analysis to develop models for directivity effects. More discussions on the data will be given in the following sections. In general, all developers' data sets included post-1995 large earthquakes not in the SSGA data set, such as the 1999 Kocaeli and Düzce, Turkey, earthquakes and the 1999 Chi-Chi, Taiwan, earthquake. Several well-recorded Chi-Chi aftershocks were included in the AS and CY data sets.

## DEVELOPMENT OF THE DIRECTIVITY MODEL

Development of our model proceeded through various stages. The first stage was data exploration, when we tried to get some general idea of what domain of the data could be fit by various directivity predictors including our chosen *IDP* above. Some earthquakes' residuals correlate well with the *IDP*, others correlate poorly, and some have strong anti-correlations, as can be seen in Figure 3, in which events are ordered by magnitude. To produce this figure a simple least-squares straight line was fit through developer AS's residuals in the 0–40 km distance bin for each earthquake for each period. Normalized slope is the slope divided by its standard deviation, which we use as an indicator of significance of the slope owing to the highly variable number of data for each quake. Recall that some events had only 4 recordings, while others had more than 100.

In general there is a positive correlation with *IDP*, shown by the predominance of open circles in Figure 3, except for a few events. The M5.99 1987 Whittier Narrows earthquake was particularly problematic, being very well recorded and showing a strong anti-correlation with *IDP*. The NGA rupture model for this event is peculiar, rupturing downward from a hypocenter exactly on the upper edge of the rupture. Small ground

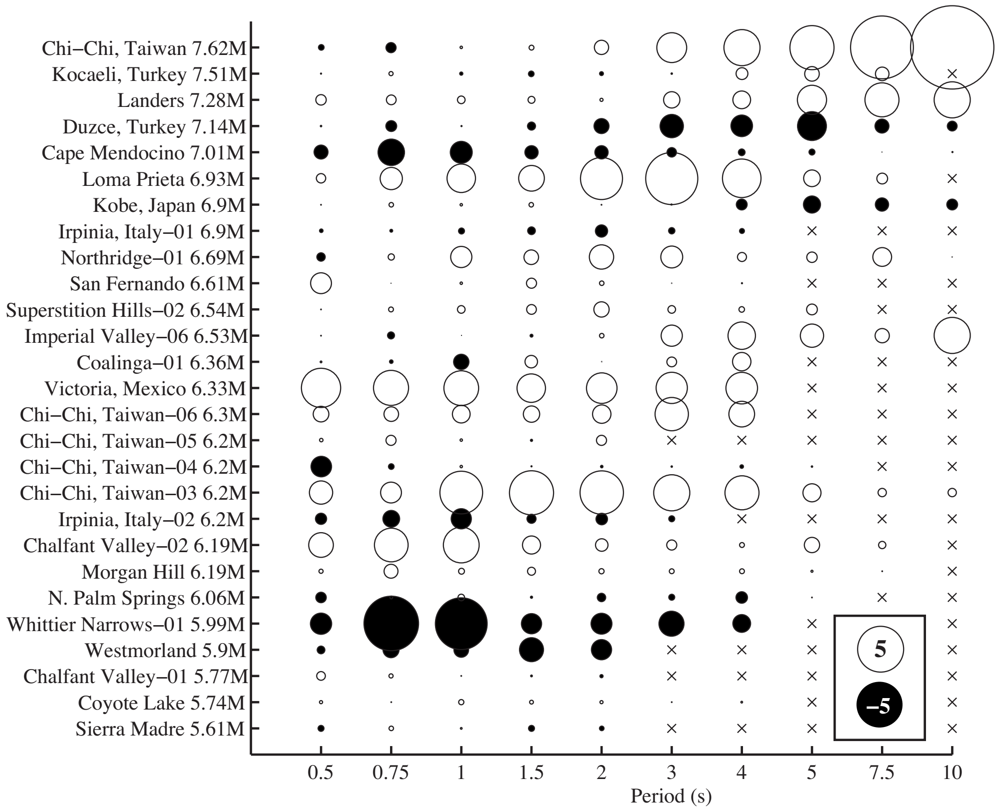


**Figure 3.** Circles show normalized slope of correlation of *IDP* with each earthquake's AS total residuals at various periods. Earthquakes are arranged in order of magnitude, indicated after earthquake name. Only data within rupture distance of 40 km are used. White/black circle indicates positive/negative slope. Circle radius proportional to slope, with slope of 5 indicated in key. × indicates a bin having fewer than 4 data.

motions at the Lamont stations that recorded the 1999 Düzce earthquake also produced a poor correlation with *IDP*.

Our general conclusion from the data exploration was that the *IDP* correlated with the developers' residuals best (i.e., had a non-zero linear slope with *IDP*) for earthquakes having $M \geq 6.0$, dips$>65°$, and periods greater than 2 sec. For near-vertical ruptures the *IDP* worked best for distances less than 40 km. For earthquakes with low dips, there was some evidence that the *IDP* correlated with the residuals better at distances beyond 40 km than shorter distances. However, for this paper we decided to concentrate on directivity in the 0–40 km range.

Based on the above observations, we formulate the directivity effect as a function of moment magnitude $M$, rupture distance $R_{RUP}$, and *IDP* as follows

$$f_D = f_r(R_{RUP})\, f_M(M)\, (a + b \cdot IDP) \tag{5}$$

Coefficients $a$ and $b$ are unknown and will be determined by regression analysis of the empirical data (developer's total residuals). $f_r$ is a distance taper, and $f_M$ is a magnitude taper, where

$$f_r = \max\left[0, \left(1 - \frac{\max(0, R_{RUP} - 40)}{30}\right)\right] \quad \text{and} \quad f_M = \min\left[1, \frac{\max(0, M - 5.6)}{0.4}\right].$$

$f_r$ has value unity for $0 \leq R_{RUP} \leq 40$ and tapers linearly to its value of zero at $R_{RUP} \geq 70$. $f_M$ has value zero for $0 \leq M \leq 5.6$ and rises linearly to its value of unity at $M \geq 6.0$.

## ESTIMATION OF THE MODEL COEFFICIENTS

For each developer team we conducted regression analysis to estimate model coefficients $a$ and $b$ for each spectral period in the list of 0.5, 0.75, 1, 1.5, 2, 3, 4, 5, 7.5, and 10 sec, the spectral periods common to the NGA models. To properly weight each event in the estimation of coefficient $a$, we used a mixed-effects model (Abrahamson and Youngs 1992; Joyner and Boore 1993). We selected as data the developer's total residuals from all earthquakes with $M \geq 6.0$ and all stations in the 0–40 km rupture distance range. Regression analysis was performed using the NLME package in the statistical software S-Plus.

Our decision to focus on the directivity effects inside the domain of $M \geq 6.0$ and $R_{RUP} \leq 40$ km required an adjustment to the NGA model residuals to account for NGA model misfits in this domain and the differences in data distribution between the developers' total data set and the data subset used in this analysis, which could upset the original event terms and hence the constant term in the NGA model. This adjustment ensured proper centering of the total residuals data and hence allows a reasonable and stable estimate of coefficient $a$ as a function of period. We did the following to make the adjustment. We fitted a mixed-effects model with a single constant term $a_o$ to developer's total residuals

$$t_i = a_o + \eta_{q(i)} + \varepsilon_i \tag{6}$$

where $t_i$ is developer's total residual for the $i$th record, and $q$ is the earthquake index for record $i$. Random variables $\varepsilon$ and $\eta$ are random errors with zero mean, the former being the record-to-record errors (the intra-event residual) and the latter being event terms. Random errors $\varepsilon$ and $\eta$ have standard deviations $\sigma_o$ and $\tau_o$, respectively. The estimated $a_o$ and $\sigma_o$ are listed in Table 2. We then subtracted the estimated $a_o$ from developer's total residuals. This adjustment was done independently for each NGA model and for each of the 10 spectral periods.

**Table 2.** Directivity model coefficients and statistics.

| Period (sec) | No. of data | No. of EQ | $a$ | $b$ | $\sigma$ | $\tau$ | $a_o$ | $\sigma_o$ | $(\sigma-\sigma_o)/\sigma_0$ |
|---|---|---|---|---|---|---|---|---|---|
| | | | | | **AS6** | | | | |
| 0.5 | 573 | 40 | 0.0000 | 0.0000 | 0.5414 | 0.2247 | 4.210E-02 | 0.5414 | 0 |
| 0.75 | 572 | 40 | −0.0447 | 0.0298 | 0.5586 | 0.2460 | −2.137E-02 | 0.5596 | 0.002 |
| 1 | 572 | 40 | −0.0765 | 0.0510 | 0.5553 | 0.3138 | 2.305E-02 | 0.5598 | 0.008 |
| 1.5 | 562 | 38 | −0.1213 | 0.0809 | 0.5174 | 0.3260 | 3.380E-02 | 0.5225 | 0.01 |
| 2 | 538 | 38 | −0.1531 | 0.1020 | 0.5240 | 0.3711 | 4.692E-02 | 0.5341 | 0.019 |
| 3 | 465 | 35 | −0.1979 | 0.1319 | 0.5178 | 0.3595 | 3.191E-02 | 0.5393 | 0.04 |
| 4 | 436 | 34 | −0.2296 | 0.1530 | 0.5294 | 0.3922 | 6.307E-02 | 0.5506 | 0.039 |
| 5 | 328 | 30 | −0.2542 | 0.1695 | 0.5285 | 0.4192 | 8.158E-02 | 0.5510 | 0.041 |
| 7.5 | 276 | 28 | −0.3636 | 0.2411 | 0.5147 | 0.4332 | −5.407E-02 | 0.5560 | 0.074 |
| 10 | 158 | 17 | −0.5755 | 0.3489 | 0.5566 | 0.3656 | −1.517E-01 | 0.6626 | 0.16 |
| | | | | | **BA6** | | | | |
| 0.5 | 419 | 27 | 0.0000 | 0.0000 | 0.5212 | 0.1945 | −8.870E-03 | 0.5212 | 0 |
| 0.75 | 418 | 27 | −0.0532 | 0.0355 | 0.5387 | 0.2618 | −3.463E-03 | 0.5394 | 0.001 |
| 1 | 418 | 27 | −0.0910 | 0.0607 | 0.5278 | 0.3068 | 5.466E-02 | 0.5327 | 0.009 |
| 1.5 | 412 | 26 | −0.1443 | 0.0962 | 0.5052 | 0.3214 | 8.360E-02 | 0.5091 | 0.008 |
| 2 | 390 | 25 | −0.1821 | 0.1214 | 0.5191 | 0.3815 | 9.181E-02 | 0.5301 | 0.021 |
| 3 | 371 | 25 | −0.2353 | 0.1569 | 0.5197 | 0.3985 | 3.557E-02 | 0.5484 | 0.052 |
| 4 | 363 | 25 | −0.2731 | 0.1821 | 0.5247 | 0.3637 | 3.217E-02 | 0.5559 | 0.056 |
| 5 | 263 | 20 | −0.3021 | 0.2015 | 0.5513 | 0.3801 | 2.285E-02 | 0.5973 | 0.077 |
| 7.5 | 234 | 20 | −0.4627 | 0.2727 | 0.5340 | 0.4514 | 4.121E-03 | 0.6005 | 0.111 |
| 10 | 129 | 12 | −0.8285 | 0.4141 | 0.5171 | 0.3387 | −1.210E-01 | 0.6503 | 0.205 |
| | | | | | **CB6** | | | | |
| 0.75 | 438 | 36 | 0.0000 | 0.0000 | 0.5298 | 0.2247 | 2.525E-02 | 0.5298 | 0 |
| 1 | 438 | 36 | −0.0329 | 0.0220 | 0.5234 | 0.2666 | 5.890E-02 | 0.5243 | 0.002 |
| 1.5 | 431 | 34 | −0.0795 | 0.0530 | 0.4889 | 0.2699 | 8.493E-02 | 0.4899 | 0.002 |
| 2 | 409 | 34 | −0.1125 | 0.0750 | 0.4921 | 0.2507 | 7.915E-02 | 0.4972 | 0.01 |
| 3 | 387 | 31 | −0.1590 | 0.1060 | 0.4964 | 0.2556 | 5.891E-02 | 0.5129 | 0.032 |
| 4 | 379 | 31 | −0.1921 | 0.1280 | 0.5075 | 0.2323 | 8.163E-03 | 0.5250 | 0.033 |
| 5 | 276 | 27 | −0.2172 | 0.1450 | 0.5206 | 0.2677 | −4.461E-02 | 0.5481 | 0.05 |
| 7.5 | 248 | 27 | −0.3227 | 0.2147 | 0.5151 | 0.3580 | −8.447E-02 | 0.5613 | 0.082 |
| 10 | 129 | 16 | −0.6419 | 0.3522 | 0.5365 | 0.4071 | −2.105E-01 | 0.6497 | 0.174 |
| | | | | | **CY6** | | | | |
| 0.75 | 570 | 40 | 0.0000 | 0.0000 | 0.5428 | 0.3615 | 8.438E-02 | 0.5428 | 0 |
| 1 | 570 | 40 | −0.0260 | 0.0200 | 0.5393 | 0.4042 | 8.660E-02 | 0.5404 | 0.002 |
| 1.5 | 560 | 38 | −0.0627 | 0.0482 | 0.5097 | 0.3998 | 9.405E-02 | 0.5113 | 0.003 |
| 2 | 536 | 38 | −0.0887 | 0.0682 | 0.5307 | 0.4044 | 1.002E-01 | 0.5349 | 0.008 |
| 3 | 462 | 35 | −0.1254 | 0.0965 | 0.5311 | 0.4335 | 1.064E-01 | 0.5431 | 0.022 |
| 4 | 432 | 34 | −0.1514 | 0.1165 | 0.5503 | 0.4274 | 1.389E-01 | 0.5626 | 0.022 |
| 5 | 324 | 30 | −0.1715 | 0.1320 | 0.5527 | 0.4895 | 5.773E-02 | 0.5655 | 0.023 |
| 7.5 | 272 | 28 | −0.2797 | 0.1865 | 0.5476 | 0.4693 | 5.731E-02 | 0.5713 | 0.041 |
| 10 | 154 | 17 | −0.4847 | 0.2933 | 0.5819 | 0.3077 | 1.719E-02 | 0.6454 | 0.098 |

Using the adjusted total residuals, we estimated coefficients $a$ and $b$ using Equation 7,

$$t_i - a_o = (a + b \cdot IDP_i) + \eta_{q(i)} + \varepsilon_i \quad (7)$$

where $a_o$ is the correction explained above, $\eta$ and $\varepsilon$ are random variables with zero mean and standard deviations $\tau$ and $\sigma$, respectively. There is no need for the tapers $f_r$ and $f_M$ in Equation 7 given that we used data only having $\mathrm{M} \geq 6$ and $R_{RUP} \leq 40$ km. Equation 6 can be considered as the null model of Equation 7 and the differences in $\sigma$ between Equations 7 and 6 can be viewed as a measure of the significance of directivity in the selected dataset.

To ensure a smooth directivity effect, we smoothed the estimated coefficients $a$ and $b$ over periods in two steps. Coefficient $b$ was smoothed first. We required the smoothed value to be non-negative because negative $b$ is anti-directivity, which our model does not predict and we do not understand. In the second step we developed a revised estimate of $a$ using Equation 7 again, but with $b$ fixed at its smoothed value from step 1. The resulting $a$ estimates were smoothed over periods with the constraint that $a$ equaled zero where $b$ equaled zero, because a non-zero $a$ in that circumstance causes a constant bias to all predicted motions. The final, smoothed coefficients $a$ and $b$ for each of the 10 periods for each developer's model are given in Table 2, along with $\tau$ and $\sigma$ from the 2$^{nd}$ step of smoothing. Plots of the original estimated values and the smoothed curves for coefficients $a$ and $b$ are shown in Electronic Appendix B (Spudich and Chiou 2008). The four resulting directivity models are called AS6, BA6, CB6, and CY6. Figure 4 shows the predicted directivity effect $f_D$ as a function of period for each of the models. They will be discussed later.

Figures 5–7 show examples of the data fit for 3, 5, and 10 sec, respectively; the fitted lines have a slope given by the smoothed $b$ and smoothed intercept $a$ (Table 2). Electronic Appendix B (Spudich and Chiou 2008) shows figures like Figures 5–7 for all periods and developers. Although the residual data in Figure 7 could be fit more closely using a bilinear function that is flat below $IDP=2$ and rises linearly above that $IDP$, we decided not to use the bilinear form for the following reasons. The high residuals in Figure 7 around $IDP=3$ at 7.5 and 10 sec are dominated by Chi-Chi stations close to the slip maximum at the northwest end of the rupture, and thus are biased high by the particular slip distribution. In addition, drop-out of a number of low non-Chi-Chi residuals at $IDP \sim 0.5$ going from 5 to 10 sec helps transform a linear trend into a bilinear trend. (This is more clearly seen in Electronic Appendix C (Spudich and Chiou 2008) residual plots for abscissa $f_D$.) Finally, we are not aware of a physical reason to justify a transition from a linear directivity at $T \leq 5$ sec to a bilinear directivity at $T \geq 7.5$ sec.

## DIRECTIVITY MODEL RESIDUALS

We have plotted our intra-event residual $\varepsilon$ from the 2$^{nd}$ step of smoothing for each developer against several independent variables, specifically 1) $v_r/\beta$, the ratio of rupture velocity to shear velocity for each earthquake, 2) distance $D$ between the hypocenter and the closest point, 3) fault dip angle, 4) magnitude, 5) predicted directivity effect $f_D$, 6)

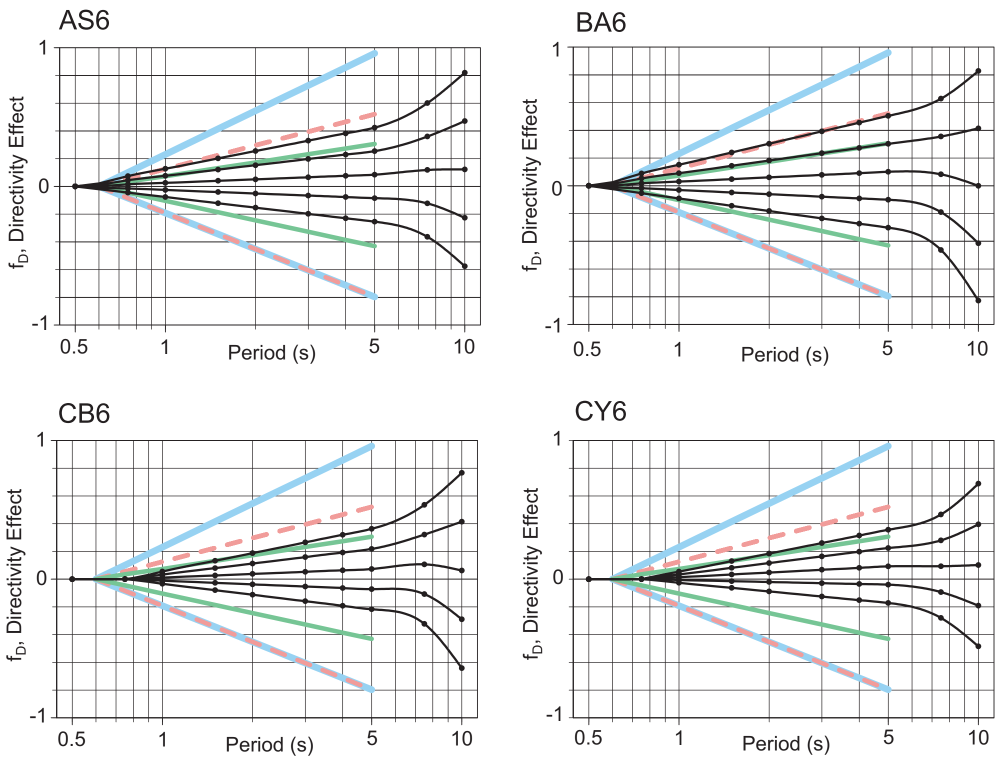


**Figure 4.** (black lines) Directivity effects predicted by the models for $IDP = 0$, 1, 2, 3, and 4. Solid blue lines are predictions for strike-slip events at $X\cos(\theta) = 0$ and 1 using SSGA; green lines are predictions for reverse events at the same values of $Y\cos(\phi)$. Dashed red lines are the predictions from strike-slip events from Abrahamson (2000).

station categorization (footwall, hanging wall, neutral zone, and other), 7) earthquake slip rake, 8) station $V_{S30}$, 9) Joyner-Boore distance, 10) closest distance to fault ($R_{RUP}$), 11) along-strike distance $s$, and 12) down-dip hypocentral distance $h$. All these plots for all directivity models are shown in Electronic Appendix C (Spudich and Chiou 2008). The data set for each plot consists of all records used by each developer for earthquakes having $\mathbf{M} \geq 6.0$ and $R_{RUP} \leq 40$ km.

The two most noticeable trends in residuals are summarized in Figure 8 for periods 3 sec and 7.5 sec. First, long-period motions ($T = 7.5$ sec) of hanging wall stations are on average underpredicted after we corrected for directivity effects. We have not yet determined how much of the underprediction is due to misfits in the developers' residuals themselves. There is also an over-prediction of neutral zone motion at 7.5 sec. Second, within each group of stations there is a distance dependence in the residuals, with residuals at large $R_{RUP}$ usually being greater than those at small $R_{RUP}$. This can be seen most clearly in the expanded plots in Electronic Appendix C (Spudich and Chiou 2008). Again, we have not yet determined how much of observed trend is from the developers'

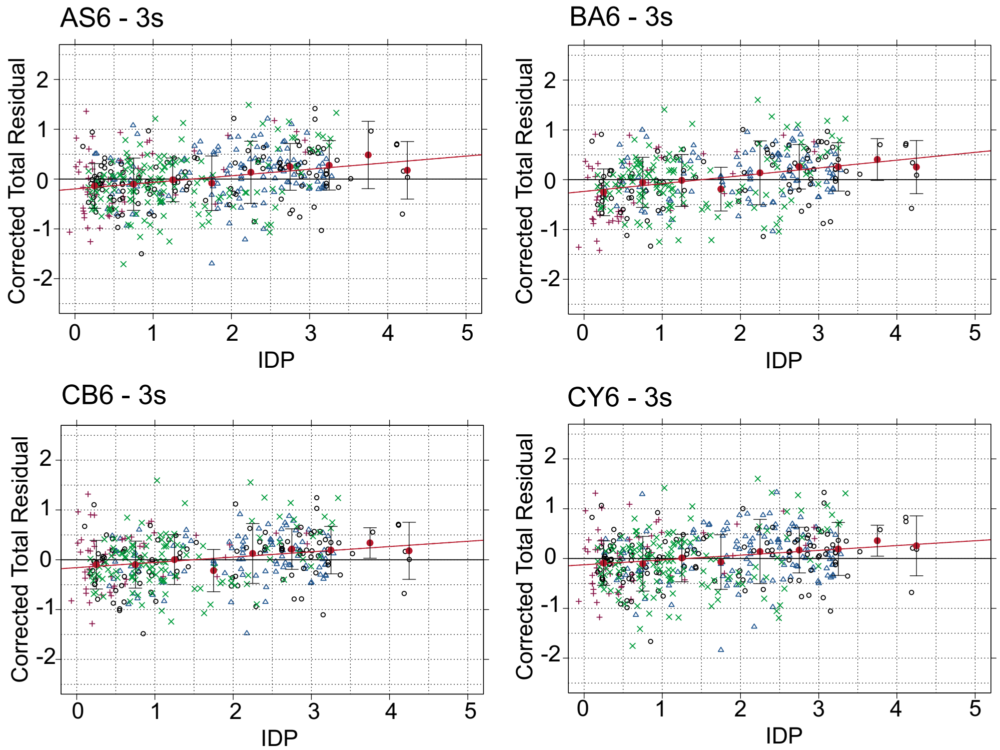


**Figure 5.** Comparison of our corrected total residuals $t$-$a_o$ with *IDP* for all developers for 3 sec period in the 0–40 km distance and M ≥ 6.0 bin. Symbols: (△) footwall stations, (+) hanging wall stations, (×) neutral zone stations, and (○) other stations (strike-slip stations), sloping line is ($a+b\cdot IDP$), and dots with error bars are means and standard deviations in adjacent *IDP* bins.

residuals themselves. However, it is important to note in Figure 8 the large negative strike-slip residuals (circles) at $R_{RUP} < 3$ km for all developers at 7.5 sec. These are for 1979 Imperial Valley stations Aeropuerto, Agrarias, and Meloland, and for 1995 Kobe stations KJMA and Kobe University. If we derived a directivity effect from strike-slip data in a $R_{RUP} < 3$ km bin, these data would imply a strong directivity effect, as has been noted by Rowshandel (2008). However, we chose not to make our directivity effect a strong function of rupture distance because these are only a few data from two earthquakes. There is no clear physical reason why directivity should be particularly strong in such a narrow zone near a rupture, particularly considering that neither earthquake had much surface faulting.

Figure 9 shows the distribution of directivity residuals as a function of $f_D$ for a subset of periods. At periods less than 5 sec, directivity residuals show no striking trends or nonuniformities, like the left column of Figure 9. However, for periods of 7.5 and 10 sec, directivity residuals tend to have a U shape. The clouds of footwall stations comprising the left and right sides of the U are Chi-Chi stations. This U shape is the residual

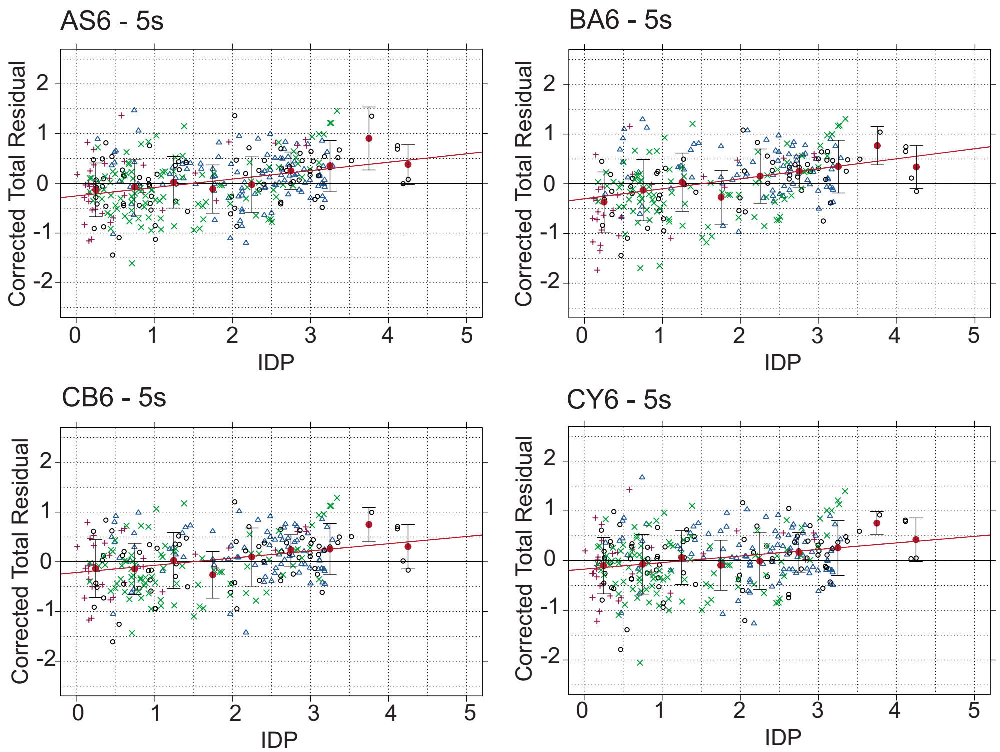


**Figure 6.** Comparison of our corrected total residuals *t*-$a_o$ with *IDP* for all developers for 5 sec period in the 0–40 km distance and M ≥ 6.0 bin. Symbols: (△) footwall stations, (+) hanging wall stations, (×) neutral zone stations, and (○) other stations (strike-slip stations), sloping line is ($a+b\cdot IDP$), and dots with error bars are means and standard deviations in adjacent *IDP* bins.

when the linear function is removed from the developer residuals, as shown for 10 sec in Figure 7. As explained earlier, we believe this U is an artifact of domination by Chi-Chi and the dropping-out of Northridge, Morgan Hill, and other event records at long period.

Plots of our intra-event residuals $\varepsilon$ against other variables (Electronic Appendix C (Spudich and Chiou 2008)) show no significant correlations with rupture velocity ratio $v_r/\beta$, magnitude, $V_{S30}$, fault dip, or rake. The lack of correlation of directivity residual with $v_r/\beta$ indicates the appropriateness of using 0.8 for the average ratio of rupture velocity to shear velocity for all events. However, the NGA data set is not rich in events having a variety of rupture speeds. The directivity residuals have the previously noted correlations with rupture distance, and they show correlations with *s* and *D* at longer periods. Since *s* and *D* are components of $f_D$, these correlations with *s* and *D* are probably related to the U shape in the residuals noted above, caused by domination of Chi-Chi at long periods.

Finally, use of our directivity model reduces the record-to-record standard deviation

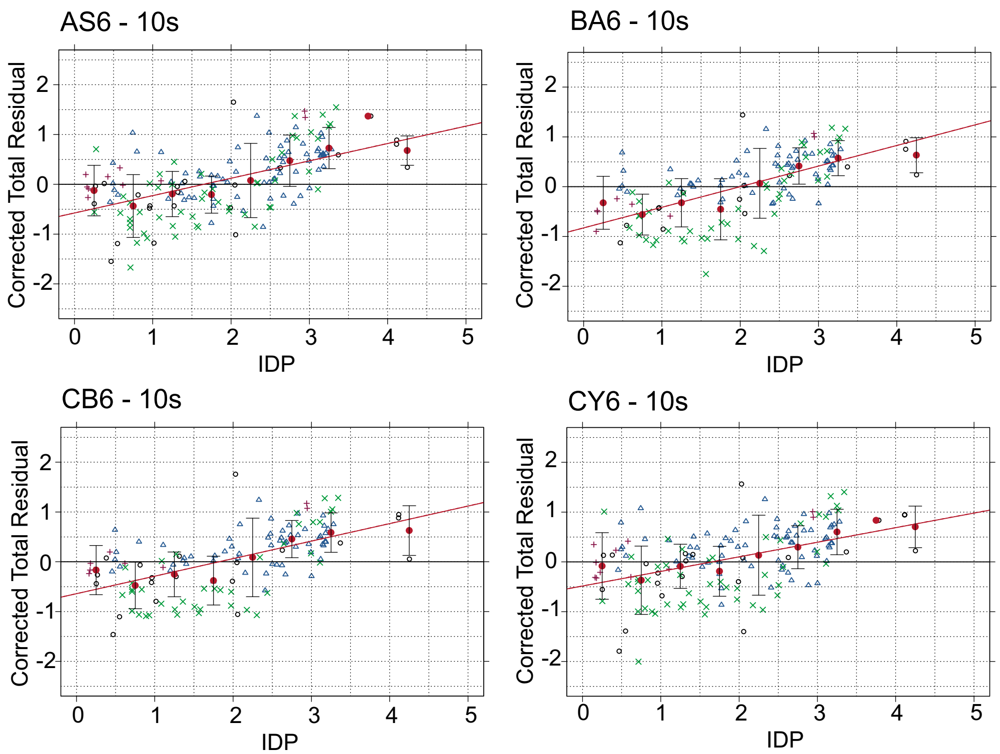


**Figure 7.** Comparison of our corrected total residuals $t\text{-}a_o$ with *IDP* for all developers for 10 sec period in the 0–40 km distance and $M \geq 6.0$ bin. Symbols: (△) footwall stations, (+) hanging wall stations, (×) neutral zone stations, and (○) other stations (strike-slip stations), sloping line is $(a + b \cdot IDP)$, and dots with error bars are means and standard deviations in adjacent *IDP* bins.

by about 16% at 10 sec, compared to a null-directivity model (Table 2). As a result of modeling directivity, the corrected NGA model's intra-event standard deviations should become smaller, but it is difficult for us to estimate the amount of reduction. The correct approach is to re-estimate the standard deviations (for both inter-event and intra-event residuals) with a directivity term in the NGA equation. However, if an interim solution for intra-event standard deviation is needed immediately, one could consult the fractions of reduction listed in Table 2, after they are smoothed over periods.

## CONCLUSIONS

In this paper we introduce a new and physically-based isochrone directivity predictor (Equation 1) and models (Equation 5 and Table 2) of directivity effects based on this predictor. Our models AS6, BA6, CB6, and CY6 almost always predict about half the directivity amplification or deamplification at every period compared to the model of SSGA, although our forward directivity is comparable to that of Abrahamson (2000), as

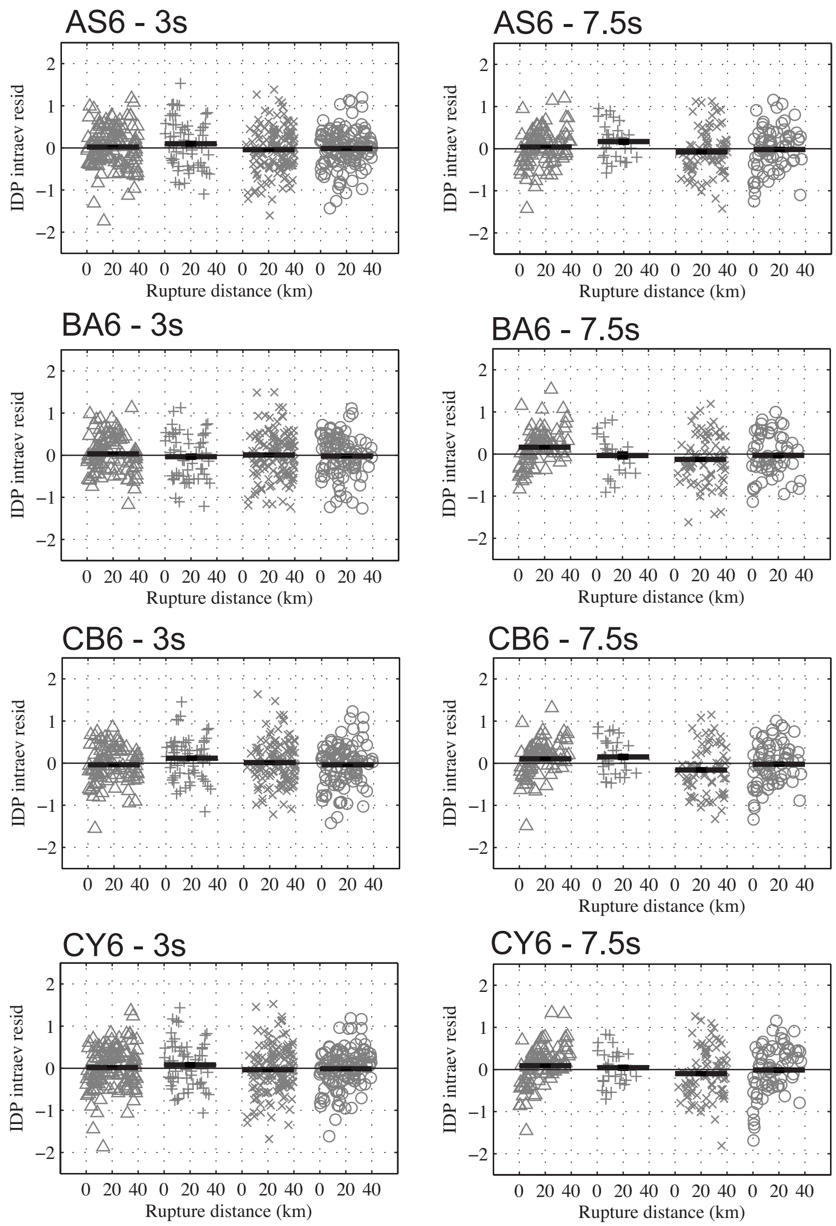


**Figure 8.** Comparison of directivity residuals with rupture distance and station classification. Data are from all events M ≥ 6.0, rupture distance <40 km. Left column: 3 sec period. Right column: 7.5 sec period. Rows from top to bottom are AS6, BA6, CB6, and CY6 directivity models. Symbols: (△) footwall stations, (+) hanging wall stations, (×) neutral zone stations, and (○) other stations (strike-slip stations). Within each box the stations are plotted according to rupture distance along a cyclic rupture distance scale. Black horizontal bars are mean values of the directivity residual, very short black vertical bars are standard errors of the mean.

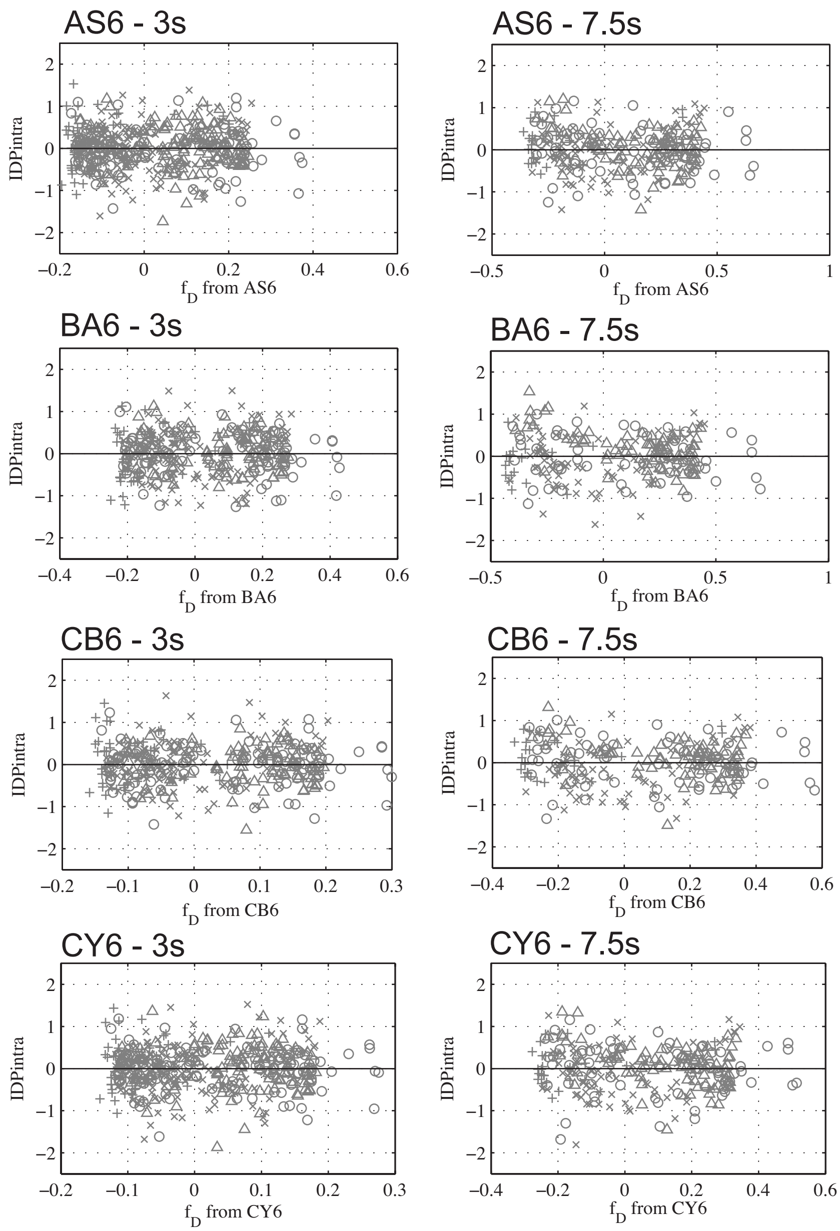


**Figure 9.** Comparison of directivity residuals with $f_D$, the predicted directivity effect. Data are from all events with M $\geq$ 6.0, rupture distance $<$40 km. Left column: 3 sec period. Right column: 7.5 sec period. Rows from top to bottom are AS6, BA6, CB6, and CY6 directivity models. Symbols: ($\triangle$) footwall stations, (+) hanging wall stations, ($\times$) neutral zone stations, and ($\bigcirc$) other stations (strike-slip stations).

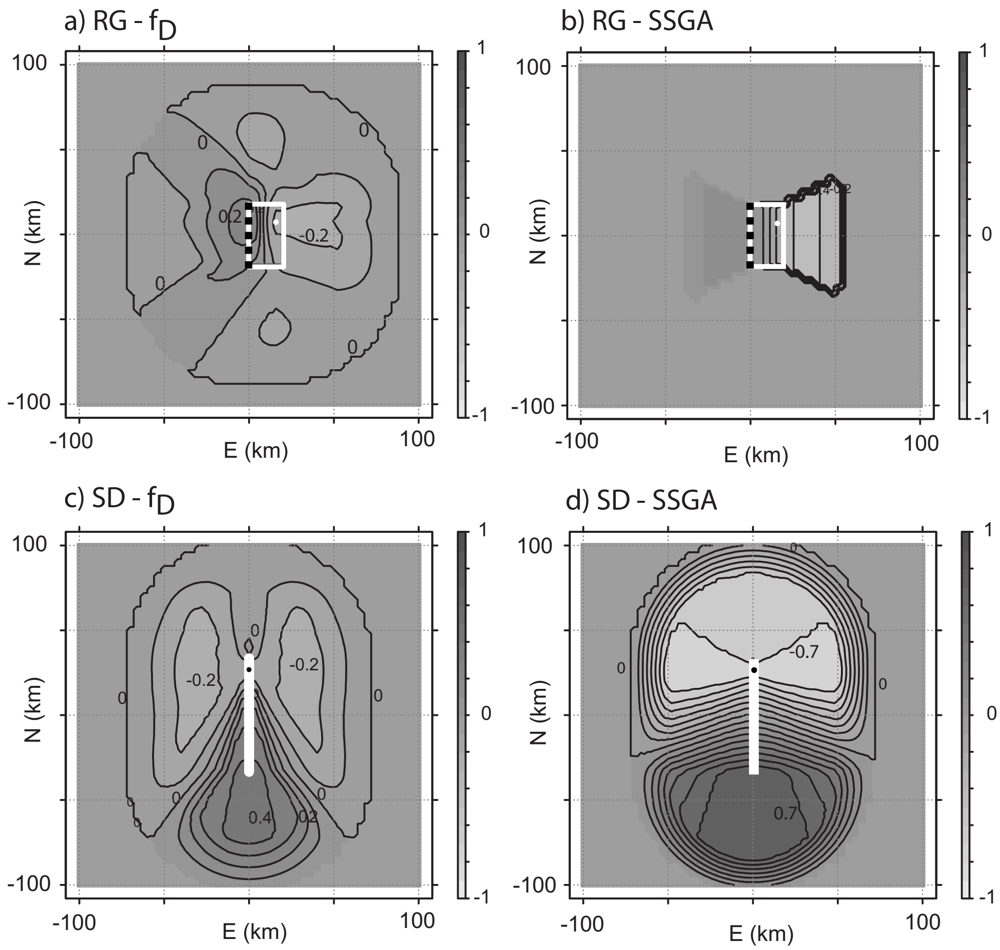


**Figure 10.** Comparison of maps of predicted directivity effect $f_D$ from AS6 (left column) and the predicted effects from SSGA (right column), both for 5 sec period. White lines show vertical projection of rupture boundaries. White or black dots indicate epicenter. Dashed line is the top edge of reverse fault. a) and b) Reverse event RG (Table 1) for AS6 and SSGA, respectively. c) and d) strike-slip event SD for AS6 and SSGA, respectively.

shown in Figure 4. Capping of the directivity predictor ($s$ by us, $X\cos(\theta)$ by Abrahamson 2000) partly contributes to the discrepancy noted at the high predictor value. Watson-Lamprey (2008) shows that the reduced scaling of directivity effects inferred from the NGA data set is caused by variations in the data set, compared to SSGA's, rather than differences of parameterization.

In addition to the difference in amplitude, maps of the predicted directivity effects (Figure 10) also reveal important spatial differences. To prepare these maps we computed directivity effects by applying the AS6 model and the SSGA model to a grid of

2601 points at a spacing of 4 km. These calculations were done for a period of 5 sec. For the vertical strike-slip fault (the geometry of event SD, Table 1), the isochrone directivity in general resembles the predictions of SSGA but predicts much narrower zones of amplification in the forward (south) direction and a small deamplification in the backward (north) direction. The maps for reverse event RG show that the isochrone directivity also resembles the pattern predicted by SSGA, but has a more gradual and natural transition going from the footwall or hanging wall zones to the neutral zones.

## ACKNOWLEDGEMENTS

This project was sponsored by the National Earthquake Hazards Reduction Program and by the Pacific Earthquake Engineering Research Center's Program of Applied Earthquake Engineering Research of Lifeline Systems supported by the California Energy Commission, California Department of Transportation, and the Pacific Gas & Electric Company. The financial support of the PEARL sponsor organizations including the Pacific Gas & Electric company, the California Energy Commission, and the California Department of Transportation is acknowledged. This work made use of Earthquake Engineering Research Centers Shared Facilities supported by the National Science Foundation under Award Number EEC-9701568. We thank D.M. Boore, K.C. Campbell, an anonymous reviewer, and all the NGA developers and stakeholders for helpful reviews and suggestions.

## LIST OF ELECTRONIC APPENDICES

Electronic Appendix A. Isochrone Theory, Generalized Geometry, and Examples

Electronic Appendix B. Fits to Developer Residuals

Electronic Appendix C. Directivity Residuals vs. Various Quantities

Electronic Appendix D. Updip Directivity Residuals (Spudich and Chiou 2008)

## REFERENCES

Abrahamson, N., 2000. Effects of rupture directivity on probabilistic seismic hazard analysis, *Proceedings from the 6th International Conference on Seismic Zonation*, Palm Springs, California.

——, 2003. Draft plan for 1-D rock motion simulations, unpublished manuscript for *Next Generation Attenuation Project*, July 11, 2003.

Abrahamson, N., and Silva, W., 2007. Abrahamson & Silva NGA ground motion relations for the geometric mean horizontal component of peak and spectral ground motion parameters, *PEER Report*, Pacific Earthquake Engineering Research Center, 378 pp.

——, 2008. Summary of the Abrahamson & Silva NGA ground motion relations, *Earthquake Spectra* **24**, 67–97.

Abrahamson, N., and Youngs, W., 1992. A stable algorithm for regression analysis using the random effects model, *Bull. Seismol. Soc. Am.* **82**, 505–510.

Bernard, P., and Madariaga, R., 1984. A new asymptotic method for the modelling of near field accelerograms, *Bull. Seismol. Soc. Am.* **74**, 539–558.

Boatwright, J., and Bundock, H., 2008. The distribution of modified Mercalli intensity in the April 18, 1906, San Francisco, earthquake, *Bull. Seismol. Soc. Am.*, **98**, 890–900, DOI: 10.1785/0120060404.

Boore, D. M., and Atkinson, G. A., 2008. Ground motion prediction equations for the average horizontal component of PGA, PGV, and 5%-damped PSA at spectral periods between 0.01 s and 10.0 s, *Earthquake Spectra* **24**, 99–138.

Campbell, K. C., and Bozorgnia, Y., 2008. Campbell-Bozorgnia NGA horizontal ground motion model for PGA, PGV, PGD, and 5% damped linear elastic response spectra, *Earthquake Spectra* **24**, 139–171.

Chiou, B., and Youngs, R., 2008. An NGA model for the average horizontal component of peak ground motion and response spectra, *Earthquake Spectra* **24**, 173–215.

Joyner, W. B., and Boore, D. M., 1993. Methods for regression analysis of strong-motion data, *Bull. Seismol. Soc. Am.* **83**, 469–487.

Mai, P. M., Spudich, P., and Boatwright, J., 2005. Hypocenter locations in finite-source rupture models, *Bull. Seismol. Soc. Am.* **74**, 965–980.

Rowshandel, B., 2006. Incorporating source rupture characteristics into ground-motion hazard analysis models, *Seismol. Res. Lett.* **77**, 708–722.

——, 2008. Directivity in NGA ground motions based on four NGA relations, *Earthquake Spectra*, submitted.

Somerville, P. G., Collins, N., Graves, R., Pitarka, A., Silva, W., and Zeng, Y., 2006. Simulation of ground motion scaling characteristics for the NGA-E Project, *Proceedings of the 8th National Conference on Earthquake Engineering*, San Francisco, California.

Somerville, P. G., Smith, N. F., Graves, R. W., and Abrahamson, N. A., 1997. Modification of empirical strong ground motion attenuation relations to include the amplitude and duration effects of rupture directivity, *Seismol. Res. Lett.* **68**, 199–222.

Spudich, P., and Chiou, B. S-J., 2006. Directivity in preliminary NGA residuals, *Final Project Report for PEER Lifelines Program Task 1M01*, available at http://quake.usgs.gov/~spudich/pdfs_for_web_page/Spudich&Chiou1M01_FinalReport-v6.pdf, 49 pp.

——, 2008. See EPAPS Document No. E-EASPEF-24-112803 for electronic appendices. For more information on EPAPS, see http://www.aip.org/pubservs/epaps.html.

Spudich, P., Chiou, B. S-J., Graves, R., Collins, N., and Somerville, P. G., 2004. *A formulation of directivity for earthquake sources using isochrone theory*, *U.S. Geological Survey Open File Report 2004-1268*, available at http://pubs.usgs.gov/of/2004/1268/.

Spudich, P., and Frazer, L. N., 1984. Use of ray theory to calculate high frequency radiation from earthquake sources having spatially variable rupture velocity and stress drop, *Bull. Seismol. Soc. Am.* **74**, 2061–2082.

——, 1987. Errata, *Bull. Seismol. Soc. Am.* **77**, 2245.

Watson-Lamprey, J., 2008. Modification of ground motion prediction equations for the effects of rupture directivity, *Earthquake Spectra*, submitted.

(Received 18 July 2007; accepted 28 November 2007)